JGR Space Physics

RESEARCH ARTICLE
10.1029/2023JA031665

Data-Based Modeling of the Magnetosheath Magnetic Field

N. A. Tsyganenko[1], V. S. Semenov[1], and N. V. Erkaev[2]

[1]Department of Physics, Saint-Petersburg State University, Saint-Petersburg, Russia, [2]Institute of Computational Modelling, Siberian Branch of the Russian Academy of Sciences, Krasnoyarsk, Russian Federation

Key Points:

- A closed empirical model of the magnetosheath magnetic field is developed, based on satellite data and a flexible mathematical architecture
- Driven by interplanetary parameters and dipole tilt, the model faithfully reproduces basic features of the IMF draping around the magnetopause
- Northward (southward) IMF results in higher (lower) subsolar fields, indicating magnetic flux pile-up (stronger reconnection), respectively

Supporting Information:

Supporting Information may be found in the online version of this article.

Correspondence to:

N. A. Tsyganenko,
nikolai.tsyganenko@gmail.com;
n.tsyganenko@spbu.ru

Citation:

Tsyganenko, N. A., Semenov, V. S., & Erkaev, N. V. (2023). Data-based modeling of the magnetosheath magnetic field. *Journal of Geophysical Research: Space Physics*, *128*, e2023JA031665. https://doi.org/10.1029/2023JA031665

Received 3 MAY 2023
Accepted 2 OCT 2023

Author Contributions:

Conceptualization: N. A. Tsyganenko, V. S. Semenov
Data curation: N. A. Tsyganenko
Formal analysis: N. A. Tsyganenko, V. S. Semenov
Funding acquisition: V. S. Semenov
Investigation: N. A. Tsyganenko, N. V. Erkaev
Methodology: N. A. Tsyganenko
Project Administration: V. S. Semenov
Resources: N. A. Tsyganenko
Software: N. A. Tsyganenko
Supervision: N. A. Tsyganenko, V. S. Semenov
Validation: N. A. Tsyganenko
Visualization: N. A. Tsyganenko
Writing – original draft: N. A. Tsyganenko
Writing – review & editing: N. A. Tsyganenko, V. S. Semenov, N. V. Erkaev

Abstract A quantitative model of the magnetosheath (MS) magnetic structure is developed, using a multi-year set of Geotail, Themis, Cluster, and MMS magnetometer and plasma instrument data. The MS database is created using an identification algorithm, based on observed magnetic field magnitudes and proton densities, normalized by their concurrent interplanetary values, followed by additional filtering with the help of standard bow shock (BS) and magnetopause (MP) models. The model architecture is based on the toroidal/poloidal formalism and a coordinate system that naturally accounts for the tailward flaring of both boundaries. The magnetic field expansions include 960 free coefficients, derived by fitting the model to a grand data set, split into independent training and validation subsets with 1,291,380 and 411,933 1-min records, respectively. The model faithfully reproduces basic types of the interplanetary magnetic field (IMF) wrapping around the MP. Regular IMF sectors result in strongly dawn-dusk asymmetric draping, with much larger magnitudes at the quasi-perpendicular dusk side of BS, and weaker at the quasi-parallel dawn side, where the MS field lines are bent and dragged tailward. Except in the case of the flow-aligned IMF orientation, the subsolar field steadily grows toward the MP, and the effect is clearly IMF Bz-dependent: the field and its gradient are larger (smaller) for northward (southward) IMF B_z, implying a pile-up of the magnetic flux in the first case and stronger reconnection in the second. Model distributions of the MS field magnitude reveal local depressions, associated with polar cusps near the high-latitude limits of data coverage.

Plain Language Summary The terrestrial magnetosheath is a relatively wide transition region, separating our planet's magnetosphere from the undisturbed flow of magnetized solar wind. Due to the sudden compression of the incoming plasma flow at the bow shock and high conductivity of the magnetosheath medium, the relatively weak magnetic field of interplanetary origin undergoes abrupt compression and drapes around the magnetosphere boundary, the magnetopause. Huge amounts of archived spacecraft data accumulated in the world data centers during past decades of space flight made it possible to develop quantitative models of the magnetosheath magnetic field, based on direct in situ observations. This paper presents first results of such a modeling study, providing a closed analytical representation of the magnetosheath magnetic field, driven by input from upstream monitors of the interplanetary medium.

1. Introduction

The terrestrial magnetosheath (MS) is the principal gateway between the solar wind and the magnetosphere, where the interplanetary magnetic field (IMF) undergoes compression and reconnects with the geomagnetic field. Due to the rapidly growing coverage of that region by archived spacecraft data, it becomes possible to empirically reconstruct the MS magnetic configurations and, potentially, reveal the global reconnection pattern at the magnetopause (MP) on the basis of direct in situ observations. A traditional target of the data-based approach in the geospace modeling has been for a long time the magnetosphere as such, confined within the MP. Several endeavors were made in the past to extend the analysis into the MS, of which the most recent and advanced one is a study by Michotte de Welle et al. (2022), based on a large amount of Cluster, Double Star, Themis, and MMS data. While having successfully obtained a number of realistic draping configurations for typical cases of the IMF orientation, that work did not provide an explicit ready-to-use field model, parameterized by external input. Instead, a direct data-based method was developed to calculate the magnetic field components and map the field lines. Among earlier papers on this subject, one should mention a work by Romashets and Vandas (2019); that study was mostly theoretical, did not use any magnetometer data inside the MS, and (following Kobel and Flückiger (1994)) used a questionable assumption of a current-free magnetic field. Zhang et al. (2019) made a comprehensive data-based statistical analysis of the MS plasma and magnetic field, but no numerical models were provided either. The goal of the present work is to fill that gap by developing a closed quantitative

representation of the MS magnetic field, somewhat similar in its structure and approach to the existing models of the magnetosphere (N. Tsyganenko et al., 2021), and derive its parameters from a large pool of space observations. Due to constraints of the MS data coverage, the modeling is confined mostly to the low/midlatitude region and is limited to within distances $R \sim 20\ R_E$ on the nightside. The paper starts with a description of the model architecture in Section 2 and its parameterization in Section 3, followed in Section 4 by a detailed account of the data used in this study and their selection criteria. Section 5 is devoted to the modeling results, starting from the model validation based on an independent subset of data, and followed by presenting equatorial plots of the MS magnetic field for different orientations of the IMF. Section 6 discusses the obtained results in terms of head-on diagrams of the MS magnetic field distribution between the BS and MP, draping geometries for different cone angles, and is concluded with a Summary in Section 7. The Supporting Information S1 part includes a complete list of the model magnetic field equations, too lengthy to be included in the main text.

2. Model Architecture and Coordinate System

Following the approach adopted in recent magnetosphere models (e.g., N. Tsyganenko et al., 2021), we start from representing the magnetic field as a sum of its toroidal and poloidal parts

$$\mathbf{B}(\mathbf{r}) = \nabla\Psi_t \times \nabla\delta + \nabla \times (\nabla\Psi_p \times \nabla\delta). \tag{1}$$

The Form 1 is not only divergence-free by construction, but also fully general, that is, can describe any solenoidal field, without any restrictions on the associated electric currents (e.g., Backus, 1958). Note that, unlike in the standard formulation, here both $\nabla\Psi_t$ and $\nabla\Psi_p$ are vector-multiplied not by the radius-vector $\mathbf{r}$, but by $\nabla\delta$, where the curvilinear coordinate δ is defined (below) in such a way that it remains constant on flaring surfaces nested between the BS and MP, and similar in shape to these boundaries. While this modification retains the $\nabla \cdot \mathbf{B} = 0$ requirement, it also makes the representation Equation 1 more consistent with the modeling region geometry, such that the toroidal (poloidal) field lines become tangential (normal) to the surfaces $\delta = \text{const}$, rather than to the spheres $r = \text{const}$. Thus, the coordinate δ controls the field variation across the interspace between the BS and MP and plays the same role as the radial distance in spherical coordinates, but in a more sophisticated form:

$$\delta(r,\theta) = 1 - R_s(r,\theta)/R_{s0}, \quad \text{where} \quad R_s = r\cos^{2\alpha}(\theta/2) \tag{2}$$

Axisymmetric surfaces $\delta(r, \theta) = \text{const}$ are similar to those introduced by Shue et al. (1997) for the MP models, also used in more recent works to approximate the BS shape (e.g., Lu et al., 2019). A specific choice of the normalization parameter R_{s0} in Equation 2 has no effect on the modeling results and may be set equal to the half-sum of standoff geocentric distances to the MP and BS: $R_{s0} = (R_{MP} + R_{BS})/2$. In such a case, the coordinate δ varies from $-\delta_0$ to $+\delta_0$ between the BS and MP, respectively, where $\delta_0 = (R_{BS} - R_{MP})/(R_{BS} + R_{MP})$.

The parameter α in the second Equation 2 defines the rate of antisunward expansion of the model boundaries. Although the actual flaring rates of the MP and BS are significantly different, we adopt a common constant value $\alpha = 0.5$ for both of them. In such a case, the MP and BS are represented by a single transverse coordinate δ, which keeps the problem within a convenient analytical form. Note here that we do not attempt to include the magnetic field discontinuities associated with BS and MP surface currents, but concentrate only on the internal configuration of the MS field. Beyond the modeling region (sunward from the BS and earthward from the MP) the model field continues as a smooth extrapolation of that inside the MS, which justifies the above assumption of constant α.

The other two coordinates entering in the generating functions $\nabla\Psi_t$ and $\nabla\Psi_p$ are the polar and azimuthal angles θ and ϕ, defined as shown in Figure 1. We presume that the MS magnetic field varies more or less gradually in the directions tangential to the MP and BS, such that the angular variation of Ψ_t and Ψ_p with respect to θ and ϕ can be approximated by linear combinations of standard spherical functions with $n = \{1, \ldots, N\}$ and $m = \{0, \ldots, n\}$. Based on the above, we represent the generating functions by triple expansions with free coefficients f_{lnm} and g_{lnm}:

$$\begin{aligned}\Psi_t(r,\theta,\phi) &= \sum_{l=0}^{L}\delta^l(r,\theta)\sum_{n=1}^{N}\sum_{m=0}^{n}V_t^{(lnm)}(\theta,\phi)\\ \Psi_p(r,\theta,\phi) &= \sum_{l=0}^{L}\delta^l(r,\theta)\sum_{n=1}^{N}\sum_{m=0}^{n}V_p^{(lnm)}(\theta,\phi)\end{aligned} \tag{3}$$

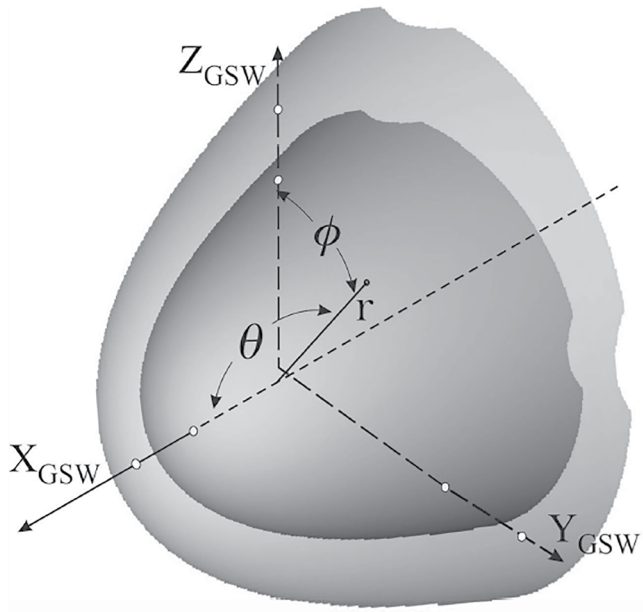

Figure 1. Coordinate system used in the MS model formulation; BS and MP surfaces are shown by gray shadings. Cartesian coordinates correspond to the GSW system with *X*-axis antiparallel to the concurrent solar wind flow.

where

$$V_t^{(lnm)} = P_n^m(\cos\theta)\left(f_{lnm}^{(t)}\cos m\phi + g_{lnm}^{(t)}\sin m\phi\right)$$
$$V_p^{(lnm)} = P_n^m(\cos\theta)\left(f_{lnm}^{(p)}\cos m\phi + g_{lnm}^{(p)}\sin m\phi\right). \quad (4)$$

Accordingly, the toroidal and poloidal magnetic field components read

$$\mathbf{B}_t = \sum_{l=0}^{L}\sum_{n=1}^{N}\sum_{m=0}^{n}\mathbf{b}_t^{(lnm)} \quad \text{and} \quad \mathbf{B}_p = \sum_{l=0}^{L}\sum_{n=1}^{N}\sum_{m=0}^{n}\mathbf{b}_p^{(lnm)}, \quad (5)$$

where the explicit forms for the partial fields $\mathbf{b}_t^{(lnm)}$ and $\mathbf{b}_p^{(lnm)}$ are rather lengthy and have therefore been relegated to the Supporting Information S1. The coefficients $f_{lnm}^{(t)}$, $g_{lnm}^{(t)}$, $f_{lnm}^{(p)}$, and $g_{lnm}^{(p)}$ entering in Equations 3–5 were further expanded into linear combinations of principal external drivers and their products, such as the IMF components, solar wind pressure, and two geodipole tilt-related terms. While more details are given in the next section; here we emphasize from the outset that the model expansions are greatly simplified by taking into account that, in the first-order approximation, contributions of individual drivers in the total magnetic field have different types of dawn-dusk and North-South symmetries and, hence, different parities with respect to Cartesian coordinates *Y* and *Z*. For example, in the case of a purely radial IMF with $B_x \neq 0$, $B_y = B_z = 0$ and normal orientation of the Earth's dipole ($\psi = 0$), the MS magnetic field should be symmetric with respect to the equatorial and meridional planes, such that (a) B_x component must be even with respect to both *Y* and *Z*, (b) B_y is odd (even) in *Y* (*Z*), and (c) B_z is even (odd) in *Y* (*Z*). Similar requirements can be formulated for all other terms, which results in a dramatic reduction of the number of non-zero coefficients to be derived from data.

The upper summation limit *L* in Equations 3 and 5 was set equal to $L = 3$; owing to differentiation in Equation 1, this is effectively equivalent, respectively, to quadratic and linear variations of the toroidal and poloidal parts between the MP and BS as a function of δ. The upper limit of the angular index *n* was set at $N = 6$, to allow for a sufficiently flexible approximation, capable to represent a variety of smooth draping geometries. As detailed in the next section, the expansion coefficients were further expanded into polynomials of principal external drivers, including the IMF components and the Earth's dipole tilt angle. Before using the model to reconstruct the actual observed fields, it was tested on artificial simulated "data," generated by an image dipole positioned inside the magnetosphere.

3. Parameterization of the Model

Following the approach developed earlier in the magnetosphere modeling (e.g., N. A. Tsyganenko & Andreeva, 2016, Section 4, and refs. therein), the amplitude coefficients $f^{(t)}_{lnm}$, $g^{(t)}_{lnm}$, $f^{(p)}_{lnm}$, and $g^{(p)}_{lnm}$ entering in Equations 3–5 were represented by polynomials of input parameters, including a solar wind pressure-dependent factor, IMF B_x, B_y, B_z, and the dipole tilt angle ψ. As a result of many experiments with different combinations of input drivers, the following generic forms have been eventually adopted, providing an apparently optimal tradeoff between the model's complexity and performance:

$$f^{(t)}_{lnm} = f^{(t,0)}_{lnm} + f^{(t,1)}_{lnm} F_P + f^{(t,2)}_{lnm} B_x + f^{(t,3)}_{lnm} B_y + f^{(t,4)}_{lnm} B_z + F_P\left[f^{(t,5)}_{lnm} B_x + f^{(t,6)}_{lnm} B_y + f^{(t,7)}_{lnm} B_z\right] + f^{(t,8)}_{lnm}\psi + f^{(t,9)}_{lnm}\psi^2 \quad (6)$$

$$g^{(t)}_{lnm} = g^{(t,0)}_{lnm} + g^{(t,1)}_{lnm} F_P + g^{(t,2)}_{lnm} B_x + g^{(t,3)}_{lnm} B_y + g^{(t,4)}_{lnm} B_z + F_P\left[g^{(t,5)}_{lnm} B_x + g^{(t,6)}_{lnm} B_y + g^{(t,7)}_{lnm} B_z\right] + g^{(t,8)}_{lnm}\psi + g^{(t,9)}_{lnm}\psi^2 \quad (7)$$

$$f^{(p)}_{lnm} = f^{(p,0)}_{lnm} + f^{(p,1)}_{lnm} F_P + f^{(p,2)}_{lnm} B_x + f^{(p,3)}_{lnm} B_y + f^{(p,4)}_{lnm} B_z + F_P\left[f^{(p,5)}_{lnm} B_x + f^{(p,6)}_{lnm} B_y + f^{(p,7)}_{lnm} B_z\right] + f^{(p,8)}_{lnm}\psi + f^{(p,9)}_{lnm}\psi^2 \quad (8)$$

$$g^{(t)}_{lnm} = g^{(p,0)}_{lnm} + g^{(p,1)}_{lnm} F_P + g^{(p,2)}_{lnm} B_x + g^{(p,3)}_{lnm} B_y + g^{(p,4)}_{lnm} B_z + F_P\left[g^{(p,5)}_{lnm} B_x + g^{(p,6)}_{lnm} B_y + g^{(p,7)}_{lnm} B_z\right] + g^{(p,8)}_{lnm}\psi + g^{(p,9)}_{lnm}\psi^2 \quad (9)$$

Each equation in Equations 6–9 contains two trinomials of IMF B_x, B_y, B_z components, the second of which is multiplied by the factor $F_P = \left(P_{\rm dyn}/\langle P_0\rangle\right)^{\chi}$, to account for a combined impact of the incoming solar wind ram pressure and IMF upon the MS magnetic field. The first and last pair of terms describe the IMF-independent effects of the pressure and dipole tilt; in regard to the latter, it was found that both linear and quadratic terms in ψ tangibly affected the model's performance and, hence, were retained in the expansions. To take into account the overall spatial compression and expansion of the MS due to varying solar wind pressure, the coordinates were scaled as $\mathbf{r}' = \mathbf{r}\left(P_{\rm dyn}/\langle P_0\rangle\right)^{\varepsilon}$. The exponents χ and ε were treated as unknown nonlinear parameters and their best-fit values were determined by minimizing the model field r.m.s. deviation from data. The obtained values $\chi = 0.56$, $\varepsilon = 0.19$ are in good agreement with theoretically expected ones, equal to 0.5 and $1/6 \approx 0.17$, respectively.

At an earlier stage of this work, we tried to also include terms with Alfven or magnetosonic Mach numbers in the above expansions; however, that led to only a very minor improvement of the fitting quality and was therefore abandoned in the final version. A probable cause of the apparent unimportance of the Mach number M_A can be the fact that $M_A \propto P^{1/2}_{\rm dyn}/B$, whereas the effects of $P^{1/2}_{\rm dyn}$ and IMF B are already included in the above model expansions Equations 6–9, which indirectly lowers the M_A influence.

It should also be specially emphasized here that, formally, Equations 6–9 represent a full general structure of the coefficients, that is, without any regard to the symmetry requirements, whereas the actual expansions for individual components are much shorter. More specifically, with $L = 3$ and $N = 6$, each of the two triple sums in Equation 5 has 108 terms, each of which, in turn, is split into two subterms, containing spherical functions with cos $m\phi$ and sin $m\phi$ factors and respective coefficients $f^{(p)}_{lnm}$ and $g^{(p)}_{lnm}$. This would yield a total of $108 \times 2 \times 2 \times 10 = 4{,}320$ terms in the four Equations 6–9 and, therefore, the same number of unknown model coefficients. However, owing to the above mentioned parity constraints imposed by the symmetry properties of individual IMF-related, tilt-dependent, and free terms, only 960 of them (i.e., less than 1/4th) survive into the final model expansions as non-zero parameters to be derived from data.

4. Data

The experimental foundation of this work consists of space magnetometer and plasma instrument data from four missions, archived at the CDAWEB online resource (https://cdaweb.gsfc.nasa.gov/cdaweb/sp_phys/) and covering more than two cycles of solar activity from 1995 to 2022, as well as OMNI archive of interplanetary medium data (https://omniweb.gsfc.nasa.gov/form/omni_min_def.html) for the same period. Space magnetometer data that contributed to this study included those by Geotail (1995–2022), Themis-A, -D, -E (2007–2022), Themis-B

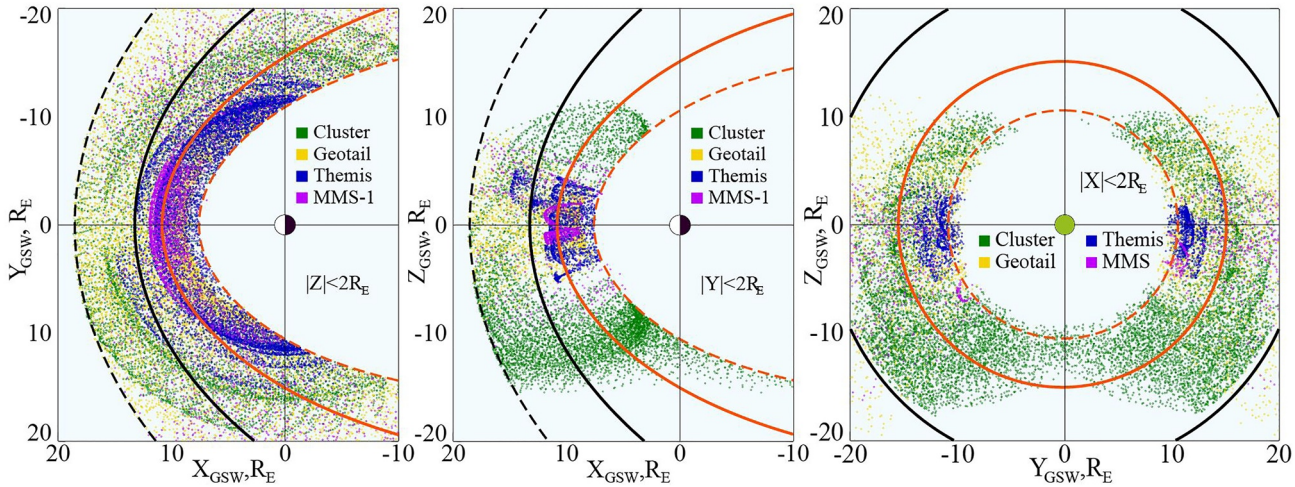

Figure 2. Spatial distribution of data records in the preliminary subset. Data of four missions are shown by different colors, as indicated in the inset legend. Only every 50th data points out of the total of 11,120,813 are plotted, limited to planar 4 R_E-thick layers centered about equatorial (left), meridional (center), and terminator (right) planes. Solid and dashed contours show, respectively, nominal and extreme positions of the MP (red) and BS (black).

and -C (2007–2010), Cluster-1, -3, -4 (2001–2021), and MMS-1 (2015–2022). After the initial visual inspection, removal of invalid records, and averaging, the magnetic field vectors were converted into GSW coordinate system with its *X*-axis aligned antiparallel to the observed solar wind direction.

Plasma data used in this work are represented by those from CIS/CODIF instruments of Cluster, electrostatic analyzer (ESA) of Themis, Comprehensive Plasma Instrument (CPI) of Geotail, and Fast Plasma Instrument (FPI) of MMS-1. Their inclusion was motivated by the need to accurately select the data taken in the MS, which is by no means a straightforward task, given extremely variable and hardly predictable instantaneous positions of the MP and BS, further complicated by a relatively narrow transverse extent of the MS between its boundaries. The existing MP and BS models, such as those of Lin et al. (2010) and Lu et al. (2019), are of little help in this sense, since they give only average positions of the boundaries and cannot accurately predict their dynamics. For that reason, a selection based solely on those models would inevitably result in gross contamination of the MS data with observations made in the magnetosphere and in the solar wind. An efficient method to discriminate between the data belonging to different regions was suggested by Jelínek et al. (2012); its essence is to construct a 2D diagram of data density, binned into intervals of observed magnetic field magnitude B and ion density D, normalized by concurrent values of the corresponding solar wind parameters, B_{sw} and D_{sw}. In thus obtained diagrams, three regions belonging to the solar wind, magnetosheath, and magnetosphere can be readily identified and separated. Due to significant differences in the orbital parameters of individual spacecraft that contributed to this study, the method by Jelínek et al. (2012) was separately applied to each of the four mission data subsets.

At the initial stage of the data processing, the 1-min average records with magnetic field and proton density values were (a) merged with concurrent OMNI interplanetary parameter records and (b) underwent a preliminary spatial filtering, such that only those data were retained for further analysis that fell between the abnormally remote BS (radially inflated by a factor 1.4) and compressed MP (radially compressed by the same factor). Figure 2 illustrates the spatial distribution of thus selected data in projections on the equatorial, meridional, and terminator planes. To avoid the excessive crowding of data points, only records falling within 4 R_E-thick layers about the corresponding planes were included in the diagrams, and only every 50th of them (out of total 11,120,813) were plotted. The nominal and extreme positions of the BS (black) and MP (red) boundaries are shown with heavy and dashed lines, respectively.

The plots reveal a significantly non-uniform coverage of the MS at low and high magnetospheric latitudes, with a certain predominance of low-latitude data. At high latitudes the data (mostly, from Cluster) are limited almost exclusively to the dayside, extending not far beyond the outer cusps. Also, the coverage is asymmetric in the North-South direction with largely prevailing data from the Southern hemispace, also contributed mainly by Cluster satellites with apogees lying below the equatorial plane.

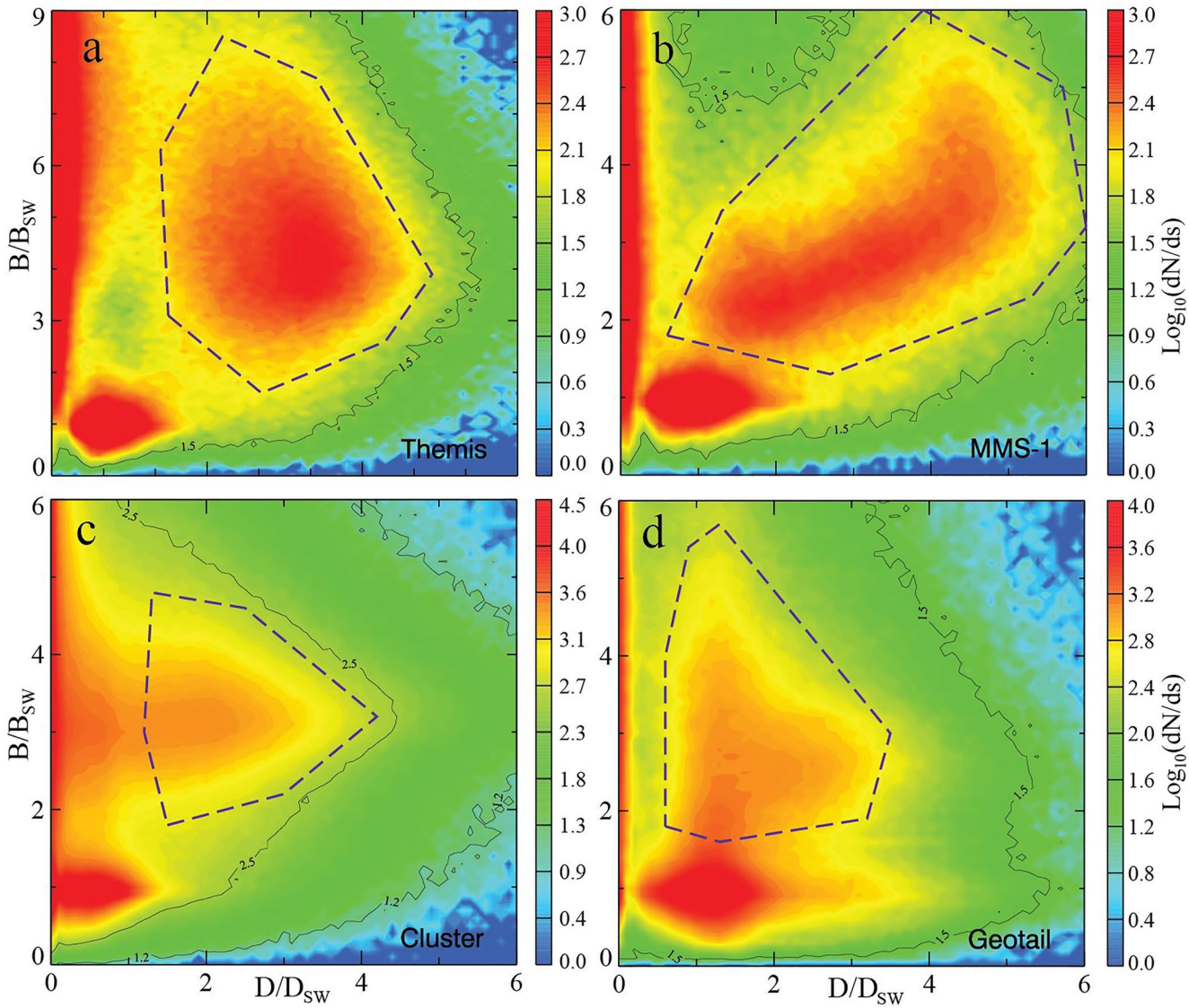

Figure 3. Distributions of all mission data shown in Figure 2 in the 2D space $D/D_{sw} - B/B_{sw}$. The color coding reflects the data density expressed via the logarithm of number of records falling into 0.1×0.1 bins of the relative proton density and magnetic field intensity. The polygons shown by heavy broken line delineate regions where the MS modeling data were selected from. Panels (a), (b), (c), and (d) correspond to Themis A–E, MMS-1, Cluster 1, 3, 4, and Geotail data, respectively.

At the next stage, the data underwent the selection based on the $D/D_{sw} - B/B_{sw}$ diagrams, following the method of Jelínek et al. (2012). Figure 3 displays four diagrams, corresponding to each of the four missions. Two top panels, a and b, display the results of binning Themis (left) and MMS (right) data, where the distinction between three physically different regions is the most pronounced.

The relatively narrow red vertical bands at the left edge of each panel correspond to the magnetospheric data, the oval-shaped spots in the left corner, centered around $D/D_{sw} \sim 1$ and $B/B_{sw} \sim 1$, originate from the solar wind observations, and the large areas enclosed within dashed-lined polygons correspond to the magnetosheath. Two bottom panels are plotted in the same format and display Cluster (c) and Geotail (d) data; one immediately notices much less clear separation between the MS and magnetosphere in the case of Cluster and a similar incomplete disconnection between the MS and solar wind in the case of Geotail.

These features reflect a significant difference in the orbital parameters of the individual missions, which justifies the separate processing of their data. Most of Themis data belong to A, D, and E probes with apogees

Table 1
MS Data Set: Contributing Missions, GSW Latitude/Longitude Range, Numbers of Records, Timespans

Mission	Lat min (degs)	Lat max (degs)	Lon min (degs)	Lon max (degs)	Number of records	Begin date (year/doy)	End date (year/doy)
Geotail	−65.7	50.8	−124.4	141.9	393,468	1995/006	2019/164
Cluster 1	−81.9	78.3	−108.9	125.2	75,451	2001/033	2004/170
Cluster 3	−84.6	72.6	−115.5	131.1	74,798	2001/035	2009/033
Cluster 4	−85.4	78.1	−120.5	133.7	625,710	2001/035	2021/336
Themis A	−33.4	37.3	−90.8	97.7	120,431	2008/142	2022/147
Themis B	−33.5	25.4	−112.1	111.5	4,557	2008/094	2009/358
Themis C	−29.6	21.0	−104.9	115.3	19,186	2007/139	2010/009
Themis D	−34.5	31.2	−91.9	93.2	99,359	2007/161	2022/162
Themis E	−29.7	31.1	−88.3	93.0	51,514	2007/161	2022/140
MMS–1	−57.7	35.4	−134.1	140.3	234,677	2015/245	2022/292
					Total: 1,699,161		

around 12–14 R_E, such that they cover only the nearest part of the subsolar MS, where the magnetic field is relatively strong and magnetopause transits by the spacecraft are the most abrupt. The MMS apogees, by contrast, concentrate at even lower latitudes and extend somewhat farther sunward (see Figure 2), which explains lower B/B_{sw} values and the narrower gap between the MS and SW data of MMS (panel b), in comparison with those on Themis diagram in panel a (note different vertical scales). The orbits of Cluster, unlike all other missions, reach much higher latitudes and often cross the outer polar cusps which, in a sense, can be viewed as a smooth continuation of the MS inside the magnetosphere (or vice versa). This naturally explains the existence of a rather wide "isthmus," connecting the MS and magnetosphere areas in panel c. The same reasoning applies to the case of Geotail (panel d): the isthmus between the MS and solar wind areas is associated with Geotail's high-perigee (9–10 R_E) and low-inclination orbit. During at least a few months of the year that satellite spends much time near the BS, which results in significant mixing of the solar wind and MS data.

Based on the starting set with 11,120,813 records (Figure 2) and the polygonal MS boundaries shown in Figure 3, we created an intermediate set of MS data, containing 2,019,060 1-min records. The selection method to separate data inside the polygons from those outside was based on a winding number algorithm (e.g., Hormann & Agathos, 2001). It is true that the purely visual definition of the polygons is inevitably subjective; however, first fitting runs based on data from larger polygons did not show any substantial difference in results, which supports our confidence in the method. Finally, an additional data filtering was carried out, based on Lin et al. (2010) and Lu et al. (2019) MP and BS models driven by concurrent interplanetary parameters. The purpose was to further refine the intermediate subset by taking out marginal data records, corresponding to most unusual positions of the boundaries. That resulted in a further ∼15% reduction of the MS data subset, such that it shrank to a total of 1,699,161 records in the final file. We also note in passing that preliminary model calculations using the larger intermediate subset did not reveal a significant change from results based on the final subset, other than a slightly higher r.m.s. deviation between the model and data.

Basic characteristics of the final data set, including individual mission contributions, latitude/longitude ranges, record numbers, and begin/end years/days are given in Table 1.

For the purpose of validating the model, the entire set was subsequently split into the training (T) and validation (V) subsets, with the total record numbers equal to 1,291,380 and 411,933, respectively. The T and V data were created using a simple algorithm that browses through the entire MS data set and selects records from consecutive 3 weeks into the T subset, while the following fourth-week data go into the V subset. In view of the fact that solar wind and IMF autocorrelation times are by at least an order of magnitude shorter than a week (e.g., Borovsky et al., 2019; Figure 1), the adopted procedure ensures that the T and V data are indeed independent of each other and, at the same time, nearly equally represent all years and all the four missions. This helps avoid any biases that might be caused by differences in the satellite orbits and long-term trends associated with solar cycle variations.

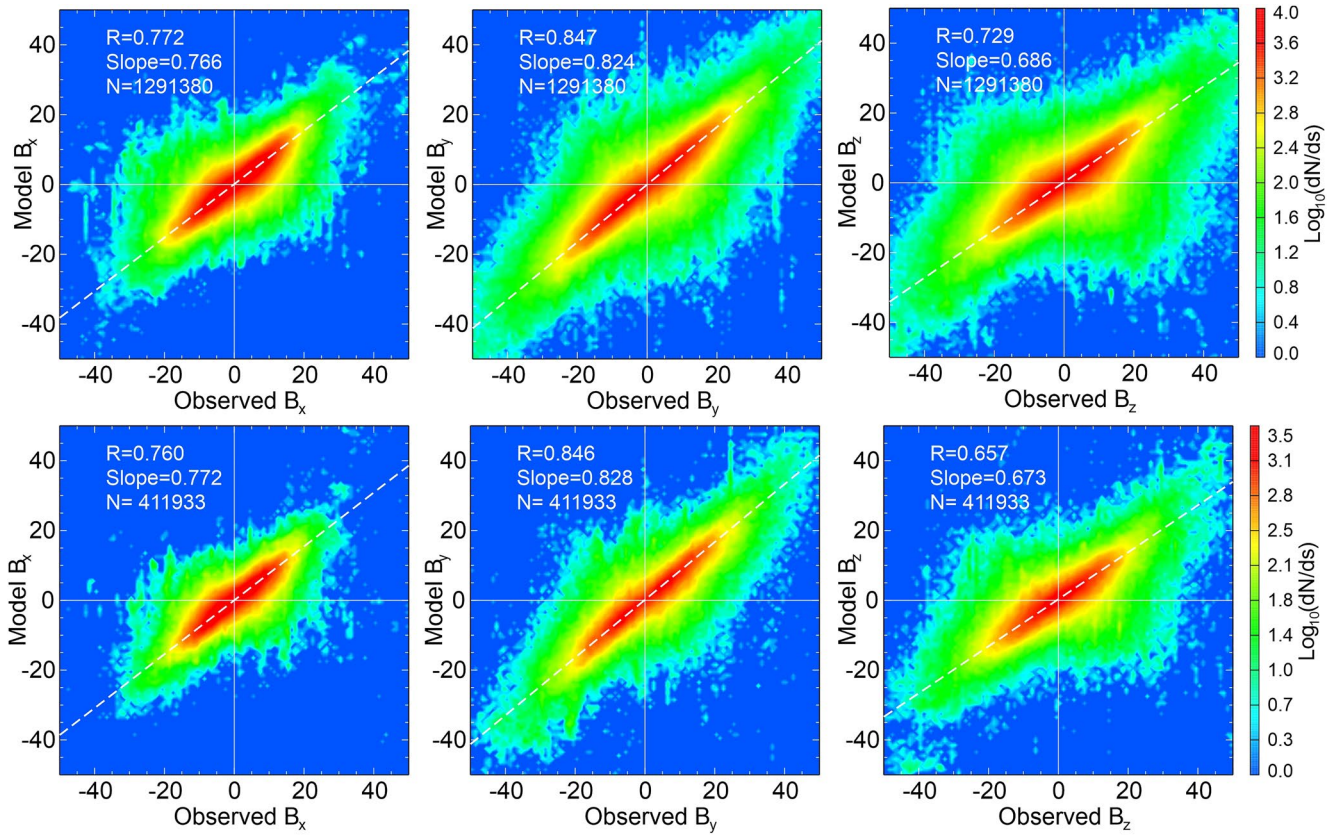

Figure 4. Diagrams illustrating the scatter between the observed and model values of three GSW components of the MS magnetic field. Plots in the top and bottom rows correspond to the training and validation subsets, respectively. Density of the data distribution about the regression lines is quantified and color-coded by logarithm of data point numbers in 1 × 1 bins of B_x, B_y, B_z values. Correlation coefficients (R), slopes, and the point numbers are indicated in legends on each panel.

5. Results

A commonly accepted measure of an empirical model performance, routinely used in previous studies, is the ratio of the r.m.s. deviation of the model field from data to the r.m.s. magnitude of the field in the modeling set:

$$Q = |\delta\mathbf{B}|_{\rm rms}/|\mathbf{B}|_{\rm rms} = \sqrt{\sum_{k=1}^{K}\left[\mathbf{B}^{(k)}_{\rm model} - \mathbf{B}^{(k)}_{\rm observed}\right]^2 \Big/ K} \Big/ \sqrt{\sum_{k=1}^{K}\left[\mathbf{B}^{(k)}_{\rm observed}\right]^2 / K} \quad (10)$$

In magnetospheric magnetic field models, typical values of Q vary in the range ~0.3–0.5 and depend on many factors, such as the size of a data set K, disturbance level, spatial extent of the modeling region, model's flexibility, etc. In the present case, the range of Q values is significantly higher due to much stronger turbulence in the MS: the above model variant fitted to the training subset yielded $Q = 0.617$, with $|\delta\mathbf{B}|_{\rm rms} = 13.65$ nT and $|\mathbf{B}|_{\rm rms} = 22.16$ nT.

Another way to evaluate the model's ability to capture observed configurations is to analyze model-data scatter plots and calculate correlation coefficients (c.c.), either for the total **B** vectors, or for each individual field component. A result of such a model-data comparison is shown in Figure 4 (top), combined with a similar set of plots for the validation subset (bottom). The highest c.c. ($R_y = 0.847$, top center panel) is found for B_y component; a natural interpretation follows from the basic IMF geometry with mostly azimuthal orientation of Parker spirals at 1 AU and alternating polarities of IMF B_y during periods of positive and negative interplanetary sectors. A lower value $R_x = 0.772$ for B_x (top left) reflects a less ordered spatial distribution of that component due to the asymmetry in the draping geometry, with oppositely directed B_x at dawn/dusk and less stable field geometry on the dawn side (see next figures below). The lowest correlation $R_z = 0.729$ for the B_z component (top right) is associated with the most irregular distribution of IMF B_z, as well as more narrow spatial extent of data in the North-South direction

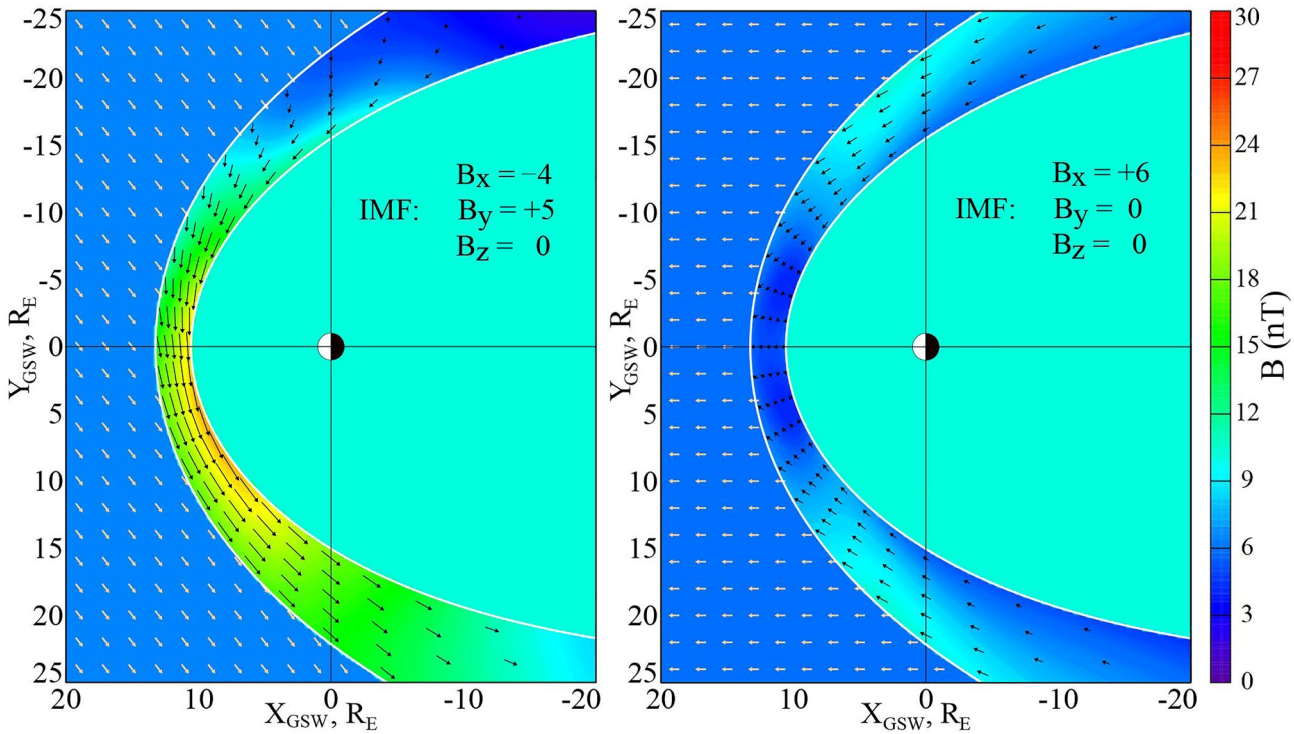

Figure 5. Equatorial distributions of the model MS magnetic field. Left: the case of a regular Parker spiral with IMF $B_x = -4$ nT, $B_y = +5$, and $B_z = 0$. Right: a purely flow-aligned IMF with $B_x = +5$ nT and $B_y = B_z = 0$.

(see Figure 2). The validation plots for the same three components are shown in the bottom panels of Figure 4; as expected, here the correlation values are somewhat lower, with the least/greatest difference in B_y (0.846 vs. 0.847) and B_z (0.657 vs. 0.729) components, respectively. The slopes of the training set regression lines vary between the highest value 0.824 for B_y and the lowest value 0.686 for B_z. For the validation set, the slopes remained virtually on the same level for B_x and B_y (0.772 and 0.828), but dropped from 0.686 to 0.673 in the case of B_z. The generally lower slope values reflect a relatively high turbulence of the MS magnetic field, which limits the accuracy of its model representation. In terms of the data scatter around the regression line, the validation plots demonstrate nearly the same degree of data ordering, in spite of being based on independent data.

The next series of plots displays equatorial distributions of the model magnetic field in the MS, combined with that in the undisturbed solar wind upstream of the BS, corresponding to the input IMF values. Figure 5 shows two equatorial model distributions of the MS magnetic field. Its left panel displays a typical case of the Parker spiral IMF with $B_x = -4$ nT, $B_y = +5$ nT, $B_z = 0$, with the other input parameters being assumed at their average nominal values: $P_{dyn} = 2.12$ nPa and $\psi = 0$. The model MP (Lin et al., 2010) and BS (Lu et al., 2019) equatorial sections are also shown with white contours; their size/shape corresponds to the same nominal input parameter values. The color coding corresponds to the full magnitude of the magnetic field, while the arrows display only equatorial projections of the total vectors onto the plotting plane. Since the magnetosphere is not covered by the modeling, the area inside the MP is uniformly colored with light blue. The most outstanding feature in the left plot is the dawn-dusk asymmetry of the MS magnetic field intensity, obviously due to the nearly tangential IMF orientation with respect to the MP and BS in the afternoon/dusk sector, in contrast to its mostly normal orientation in the prenoon/dawn sector, where the MS plasma flow sweeps the field lines tailward. Incidentally, that asymmetry can be the main cause of the residual dawn-dusk asymmetry of the Lin et al. MP model, where the equatorial dawn radius of the boundary at $X = 0$ is by ~0.5 R_E larger than at dusk. Another noteworthy detail is that the jump of the field magnitude across the BS is the most pronounced in the postnoon MLT sector, while it virtually does not exist at the morning side.

The right panel in Figure 5 shows a relatively rare case of strictly flow-aligned IMF with $B_x = +6$ nT and $B_y = B_z = 0$. Here, by contrast to the previous case, the magnetic field inside the MS is much weaker, especially in the subsolar

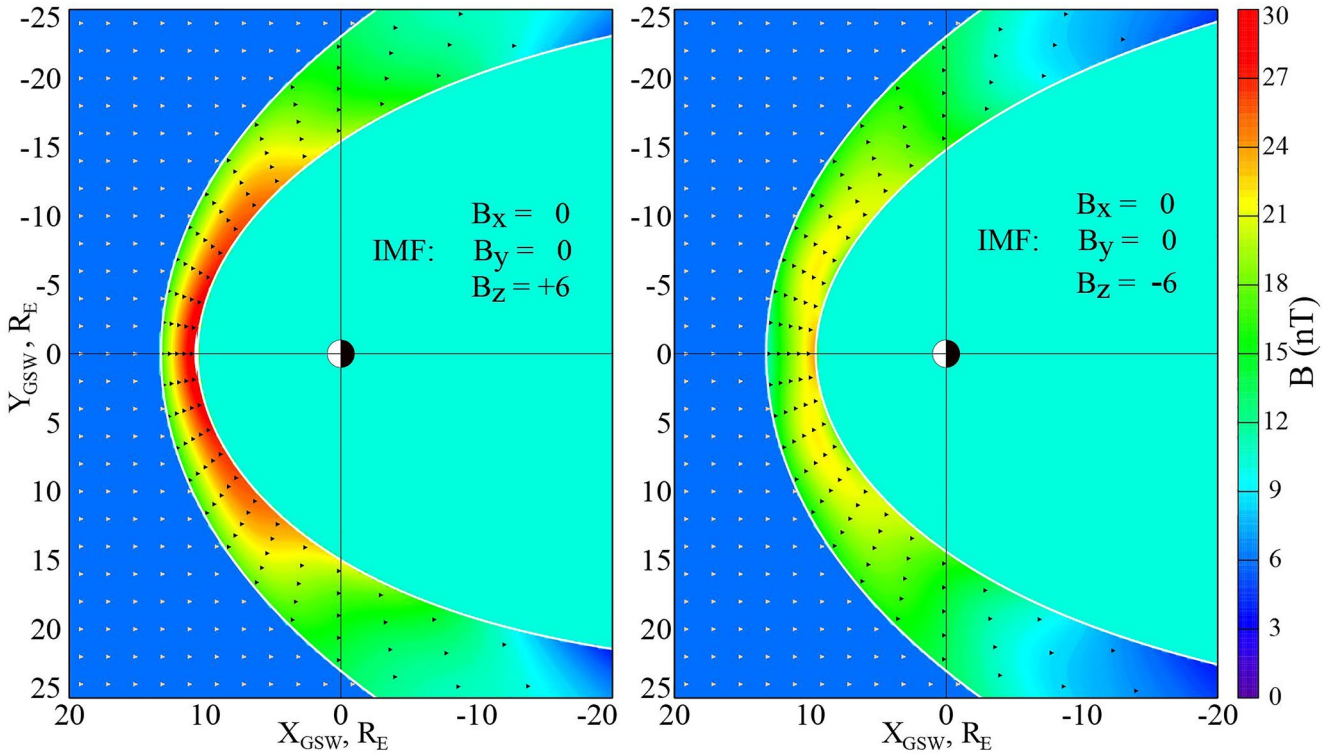

Figure 6. Same as in Figure 5 but for purely North-South IMF $B_z = +6$ nT (left) and $B_z = -6$ nT (right). In both cases $B_x = B_y = 0$. Note the significantly lower B magnitude in the right plot.

area. The field magnitude gradually increases away from the X axis, peaking at ∼8 and ∼16 hr of MLT, where the field vectors become nearly tangential to δ = const surfaces, in line with Kobel and Flückiger (1994) and MHD theory. In this case, the very weak subsolar field magnitude is a result of two factors. First, due to the flow and field symmetry, the magnetic field vector is normal to the BS in the subsolar area and, hence, its magnitude is conserved across the boundary, in line with the $\nabla \cdot \mathbf{B} = 0$ condition. Second, the plasma streamlines and, hence, the frozen-in magnetic field lines symmetrically diverge away from the Sun-Earth line, which results in a further reduction of the field magnitude along the X-axis toward the subsolar stagnation point at the MP, where the gasdynamic theory (Spreiter & Rizzi, 1974) predicts zero magnetic field. At larger angular distances from the symmetry axis, the field magnitude increases, also in agreement with the theory (see Equation 14 in the above cited paper). This is clearly seen in the right diagram of Figure 5 as the gradual color brightening in the post-dawn and pre-dusk MS sectors.

The next Figure 6 shows similar diagrams, but for purely North-South IMF, with positive $B_z = +6$ nT and negative $B_z = -6$ nT in the left and right panels, respectively. The subsolar BS positions are virtually the same in both instances, while the model MP is shifted earthward by ∼1 R_E in the case of negative IMF B_z. Nevertheless, in the latter case one clearly sees much weaker MS magnetic field over almost the entire span of dayside longitudes. A straightforward interpretation can be given in terms of reconnection: positive IMF B_z results in the stagnation and pile-up of the incoming IMF flux (e.g., Erkaev et al., 2003, 2006; Phan et al., 1994; Pudovkin & Semenov, 1985; Pudovkin et al., 2001). By contrast, negative IMF B_z initiates the classic Dungey convection, which ensures an efficient removal of the magnetic flux from the subsolar area. These effects will be illustrated in further detail in Section 6.

Figure 7 illustrates two cases of commonly observed regular IMF sector with $B_x = -4$ and $B_y = +5$, with a significant positive $B_z = +4$ (left) and negative $B_z = -4$ nT (right). As in the case with IMF $B_z = 0$ (Figure 5, left), in both instances one sees a dawn-dusk asymmetry with stronger fields in the post-noon sector. In addition, and in line with the result shown in Figure 6, the IMF B_z reversal from North to South results in a tangible decrease of the MS field magnitude.

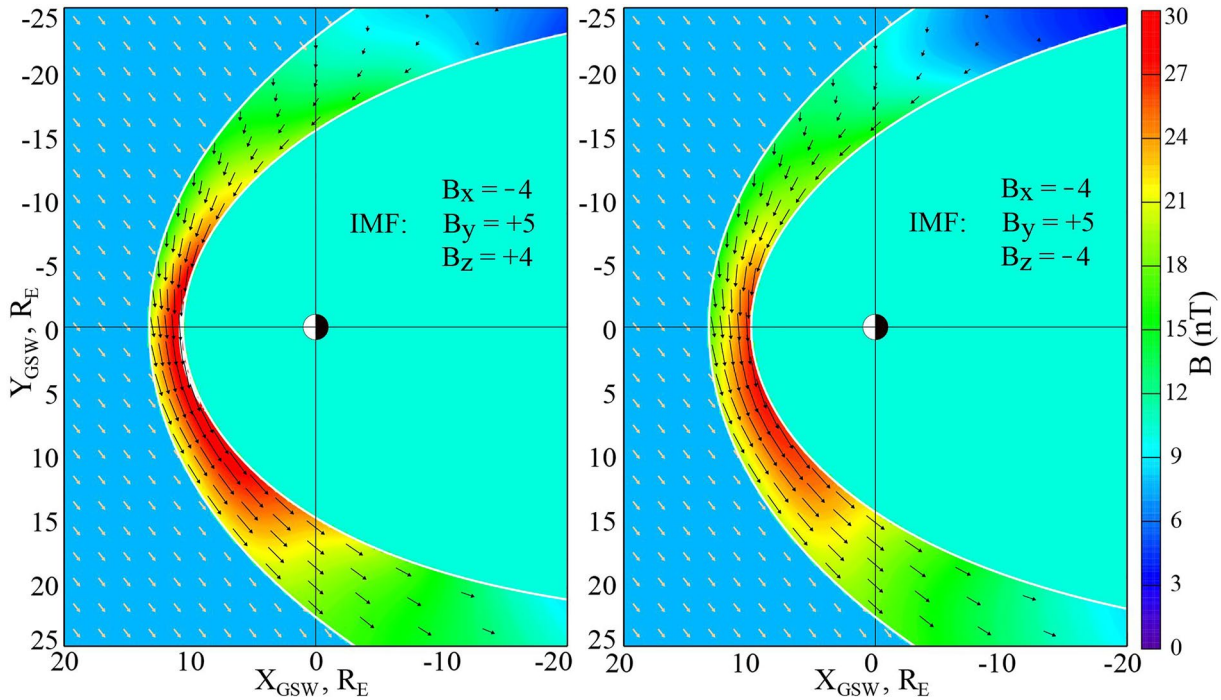

Figure 7. Draping diagrams similar to those in Figures 5 and 6, for regular negative IMF spiral sectors with $B_x = -4$, $B_y = +5$, and non-zero IMF $B_z = +4$ (left) and $B_z = -4$ nT (right).

6. Discussion

The plots in Figures 5–7 illustrated equatorial distributions of the model magnetic field. In this section we turn attention to the draping topology as viewed from the Sun, projected onto the terminator plane.

To visualize the MS magnetic field magnitude and orientation for different IMF clock angles ϕ and at different relative locations with respect to the inner (MP) and outer (BS) boundaries, the next two figures present distributions of the total $|\mathbf{B}|$ magnitude and transverse $\mathbf{B}_\perp$ vectors on two intermediate surfaces between the BS and MP. Figure 8 shows plots for an intermediate surface δ = const, lying earthward from the BS at 50% of the total distance ΔR between BS and MP, with panels (a), (b), (c), (d) corresponding, respectively, to $\phi = 0°$, 60°, 120°, and 180°.

As can be seen in the diagrams, the MS field directions almost exactly replicate those of IMF, while the field intensity varies in the range 15–25 nT and its spatial distribution changes in shape, such that the subsolar field gradually decreases with growing clock angle and reaches minimal values at $\phi = 180°$.

Figure 9 shows a distribution similar to Figure 8, but on a surface δ = const that lies much closer to the magnetopause, at the distance equal to only 10% of ΔR.

The MS field magnitude is displayed on the same color scale as in Figure 8; it has much higher values throughout a wide area in the subsolar region at $\phi = 0$ (panel a), but gradually fades away with IMF rotation and evolves into a more complex pattern at $\phi = 180°$ (panel d). In panels (b) and (c) the field vectors in the center reveal a tendency to change their orientation to more northward, most likely an average effect of reconnection with the terrestrial field. In all four panels, one can also see the polar cusp depressions as the faint blue/green spots, most clearly visible in the case of northward IMF B_z.

Figure 10 shows draping configurations for the equatorial IMF with $B_z = 0$ and four values of the IMF cone angle in the range between strictly flow-aligned and strictly quasi-perpendicular orientations. The MS field lines are shown up to their crossing points with the nominal MP.

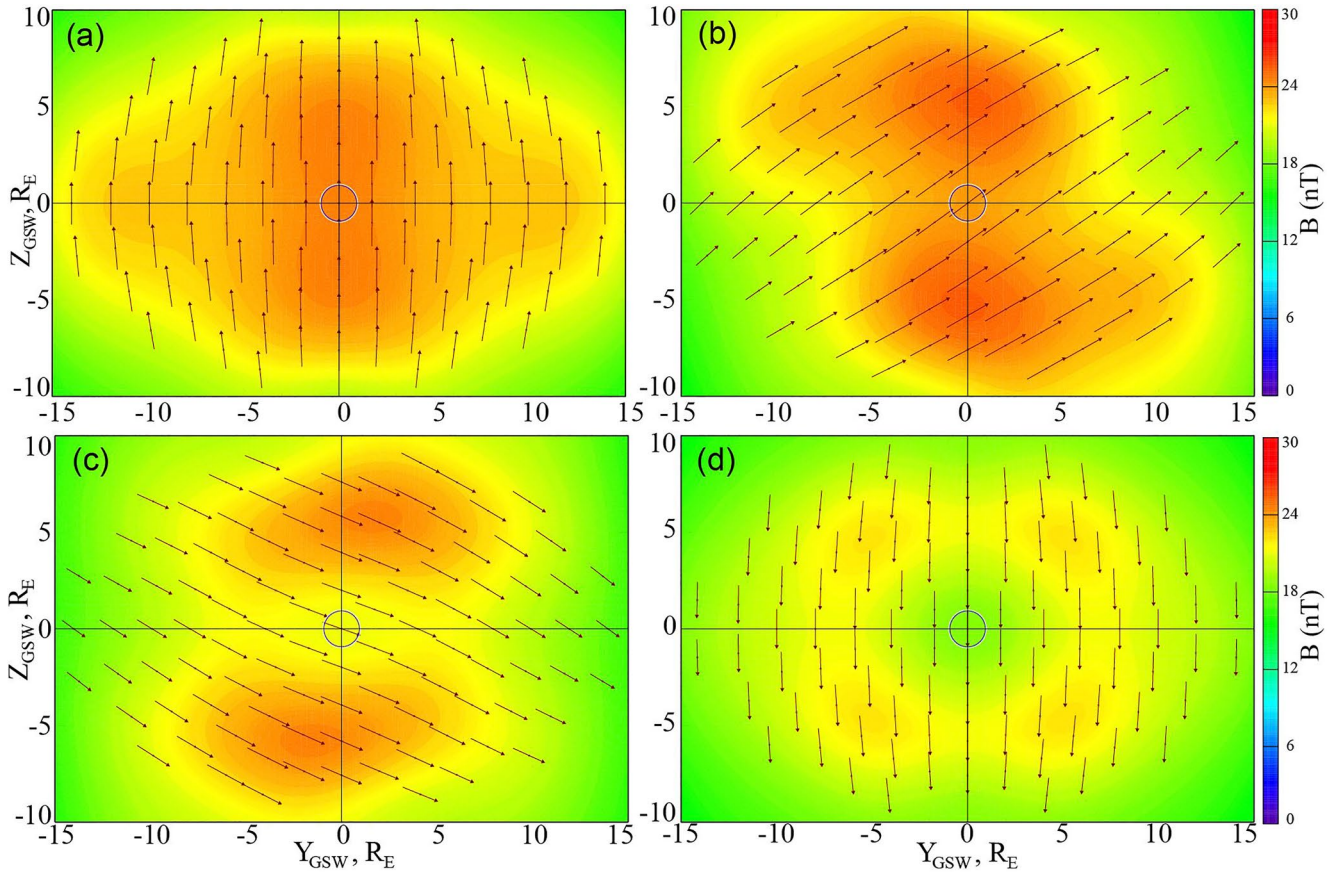

Figure 8. Distributions of the MS magnetic field on a δ = const surface, lying inward from the BS at half distance to the model MP. Four panels (a)–(d) correspond to four successive values of the IMF clock angle ϕ, from $\phi = 0$ (a) to $\phi = 180°$ (d). The color coding shows the total field intensity and the black arrows indicate the vector directions and magnitudes in projection on the plotting plane.

As already noted, the MS model field by construction smoothly extends beyond the boundaries without any abrupt jumps due to surface currents. In the case (a) with flow-aligned IMF, the field lines diverge at the subsolar point; in the case (b) with $\theta = 30°$, their dawnside shape is more complex. Namely, near the BS the magnetic field is oriented tailward, but turns sunward near the MP. The resulting arched shape of the field lines and their tailward bending may be interpreted as a result of the magnetic field sweeping by the accelerating antisunward plasma flow in the MS. Note that the same effect was found by Michotte de Welle (2022) for the case of relatively small cone angles (see their Figure 5, bottom panel), in obvious disagreement with the field geometry in a vacuum model by Kobel and Flückiger (1994) (the same paper, top panel in Figure 5). As the cone angle grows to 60°, the postnoon MS field intensity increases (c) and, in the case of strictly perpendicular IMF (d), its peak eventually becomes centered at the subsolar point.

As a final comment, we emphasize once again that the present model does not represent the current systems on the MS boundaries, and the magnetic field is smoothly extrapolated beyond the BS and MP. Adding those currents and extending the model outward is a separate attractive task for future studies, which may help understand the actual geometries of the IMF interaction with the terrestrial field and shed more light on the problem of the antiparallel versus component merging at the MP (a comprehensive list of references can be found in a recent review by Trattner et al. (2021)).

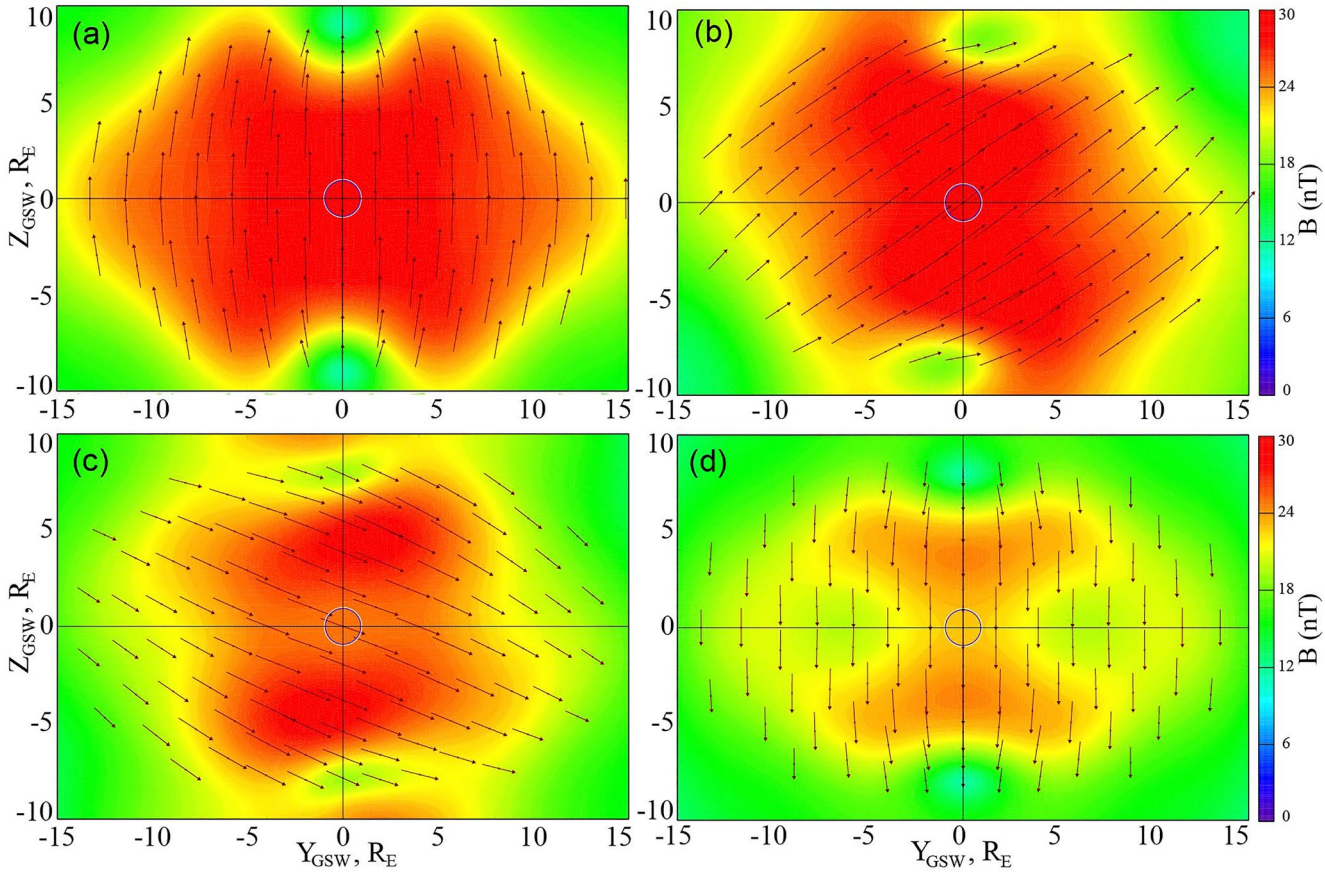

Figure 9. Same as in Figure 8, but at a δ = const surface located much closer to the MP, at 10% of the distance D between the MP and BS.

7. Summary and Outlook

In this work, we presented for the first time a closed quantitative model of the magnetosheath magnetic field, based on multi-year pool of in situ spacecraft data. The model is driven by three components of the observed IMF, solar wind dynamical pressure, and the Earth's dipole tilt angle. The model architecture is based on a general representation of the magnetic field by a sum of toroidal and poloidal components, with the corresponding generating functions Ψ_t and Ψ_p being described in "quasi-spherical" coordinates $\{\delta, \theta, \phi\}$, where δ quantifies a relative location of a point with respect to the MS boundaries. Having fitted the model to a subset of 1,291,380 1-min data records, we obtained a set of 960 coefficients, thus providing a numerical description of the MS magnetic field. The modeling region extends down to $X_{GSW} \sim -10\ R_E$ on the nightside and up to polar cusp magnetic latitudes $\pm 60°$ on the dayside. The model validation, diagrams of the MS field magnitude, and draping geometries demonstrate its faithful performance in the light of previous studies, including such features as the steady increase of B intensity toward the magnetopause, its dependence on the Parker spiral angle and IMF B_z polarity. In the case of northward orientation of IMF B_z, the MS field and its inward gradient are found to be persistently higher, which we interpret as a result of the magnetic flux pile-up on the dayside. By contrast, southward IMF results in significantly lower MS fields, naturally explained as a consequence of intensified reconnection in the subsolar area. Further studies are envisioned, with a goal to explicitly represent the electric currents on the BS and MP and thus directly reveal from data the actual IMF merging patterns at the magnetopause. Such projects will necessarily call for more sophisticated methods of data treatment, based on already existing knowledge of complex properties of plasma and magnetic fields in the solar wind (e.g., Borovsky, 2021; Borovsky et al., 2019; Němeček et al., 2020) and the magnetosheath (e.g., Dimmock et al., 2020; Zhang et al., 2019, and refs. therein).

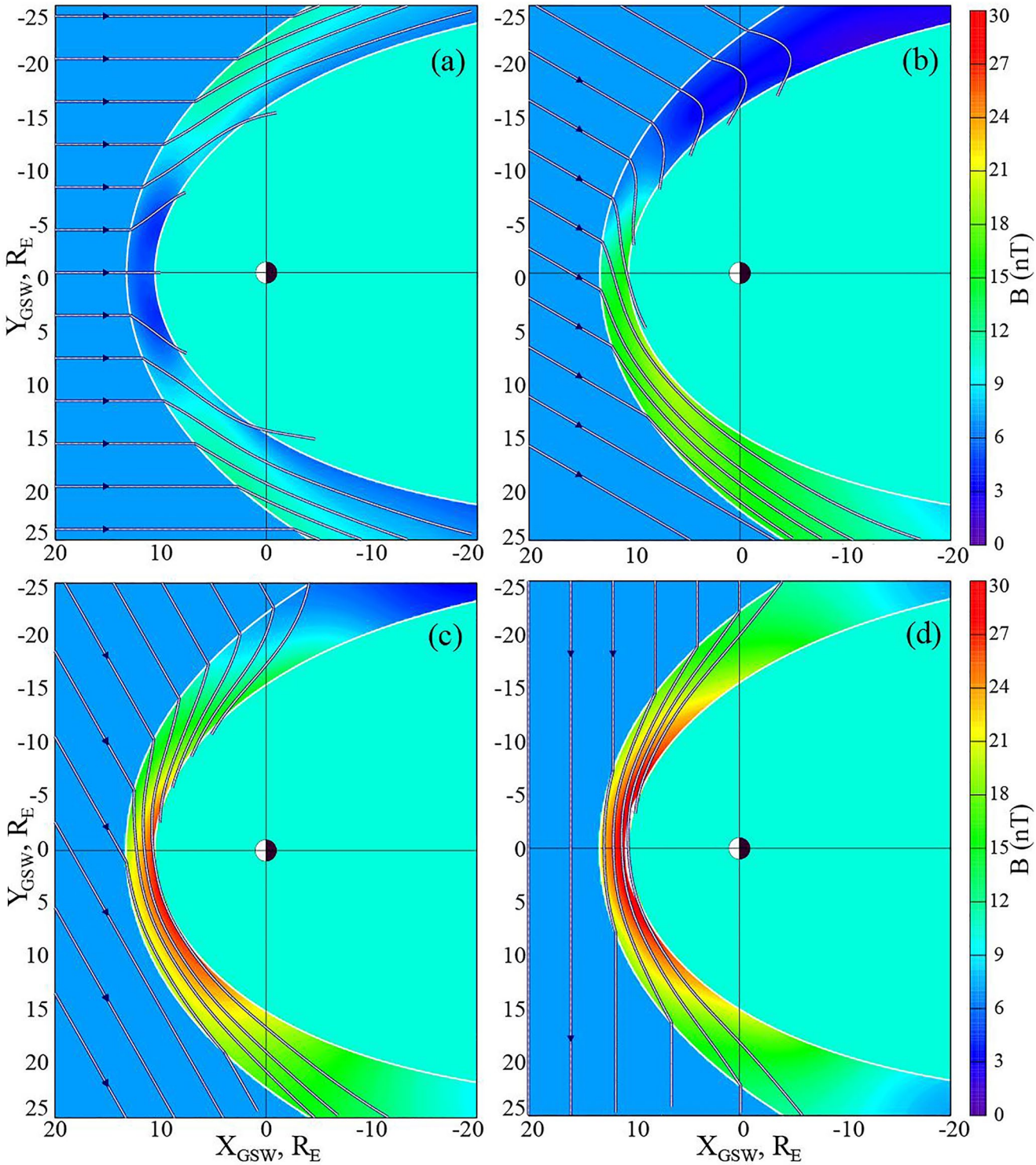

Figure 10. Magnetic field line draping in equatorial projection for four values of the IMF cone angle: $\theta = 0$ (a), $\theta = 30°$ (b), $\theta = 60°$ (c), and $\theta = 90°$ (d). In all cases, IMF $B_z = 0$ and $B = \sqrt{B_x^2 + B_y^2} = 7$nT.

Data Availability Statement

Geotail, Cluster, THEMIS, and MMS magnetometer and plasma instrument data were downloaded from the NSSDC CDAWEB interface at https://cdaweb.gsfc.nasa.gov/cdaweb/index.html. 1-min resolution OMNI data were obtained from SPDF OMNIWEB at https://omniweb.gsfc.nasa.gov. All data sets and software used to obtain the above described results are archived and made available for downloading from Zenodo repository (N. Tsyganenko et al., 2023; https://doi.org/10.5281/zenodo.8416108).

Acknowledgments

We acknowledge the teams and PIs of all experiments whose data contributed to this study. In particular, Geotail MGF data were provided by the PIs, S.Kokubun (STEL), and T. Nagai (Tokyo Institute of Technology, Japan). The Cluster and MMS magnetometer/ephemeris data were obtained from the NSSDC CDAWEB online facility, originally made available by the PIs: A. Balogh and M. Tatrallyay (Cluster data), J. Burch, C. Russell, and W. Magnus (MMS data), V. Angelopoulos, K.-H. Glassmeier, U. Auster, and W. Baumjohann are acknowledged for the use of THEMIS FGM data. High-resolution OMNI interplanetary data were obtained from the SPDF OMNIWEB interface (R. McGuire, N. Papitashvili). NT thanks Mikhail Sitnov for calling his attention to this topic. Many thanks are due to an anonymous Reviewer for the constructive criticism and, in particular, for pointing out the seminal work by Jelinek et al. (2012). We are also grateful to Victor Sergeev for his comments and suggestions made at an early stage of this project. This work is supported by the Russian Science Foundation Grant 23-47-00084 "Magnetic Reconnection in Space and Laboratory Plasmas: Computer Simulations and Empirical Modeling."

References

Backus, G. (1958). A class of self-sustaining dissipative spherical dynamos. *Annals of Physics*, *4*(4), 372–447. https://doi.org/10.1016/0003-4916(58)90054-X

Borovsky, J. E., Denton, M. H., & Smith, C. W. (2019). Some properties of the solar wind turbulence at 1 AU statistically examined in the different types of solar wind plasma. *Journal of Geophysical Research: Space Physics*, *124*(4), 2406–2424. https://doi.org/10.1029/2019JA026580

Borovsky, J. E. (2021). Solar-wind structures that are not destroyed by the action of solar-wind turbulence. *Frontiers in Astronomy and Space Sciences*, *8*. https://doi.org/10.3389/fspas.2021.721350

Dimmock, A. P., Hietala, H., & Zou, Y. (2020). Compiling magnetosheath statistical data sets under specific solar wind conditions: Lessons learnt from the Dayside Kinetic Southward IMF GEM Challenge. *Earth and Space Science*, *7*(6). https://doi.org/10.1029/2020EA001095

Erkaev, N. V., Farrugia, C. J., & Biernat, H. K. (2003). The role of the magnetic barrier in the solar wind-magnetosphere interaction. *Planetary and Space Science*, *51*(12), 745–755. https://doi.org/10.1016/S0032-0633(03)00111-9

Erkaev, N. V., Mezentsev, A., & Biernat, H. (2006). Influence of the interplanetary magnetic field on the solar wind flow about planetary obstacles. *Space Science Reviews*, *122*(1–4), 209–219. https://doi.org/10.1007/s11214-006-6059-z

Hormann, K., & Agathos, A. (2001). The point in polygon problem for arbitrary polygons. *Computational Geometry*, *20*(3), 131–144. https://doi.org/10.1016/S0925-7721(01)00012-8

Jelínek, K., Němeček, Z., & Šafránková, J. (2012). A new approach to magnetopause and bow shock modeling based on automated region identification. *Journal of Geophysical Research*, *117*(A5), A05208. https://doi.org/10.1029/2011JA017252.1

Kobel, E., & Flückiger, E. O. (1994). A model of the steady state magnetic field in the magnetosheath. *Journal of Geophysical Research*, *99*(A12), 23617–23622. https://doi.org/10.1029/94JA01778

Lin, R. L., Zhang, X. X., Liu, S. Q., Wang, Y. L., & Gong, J. C. (2010). A three-dimensional asymmetric magnetopause model. *Journal of Geophysical Research*, *115*(A4), A04207. https://doi.org/10.1029/2009JA014235

Lu, J. Y., Zhou, Y., Ma, X., Wang, M., Kabin, K., & Yuan, H. Z. (2019). Earth's bow shock: A new three-dimensional asymmetric model with dipole tilt effects. *Journal of Geophysical Research: Space Physics*, *124*(7), 5396–5407. https://doi.org/10.1029/2018JA026144

Michotte de Welle, B., Aunai, N., Nguyen, G., Lavraud, B., Génot, V., Jeandet, A., & Smets, R. (2022). Global three-dimensional draping of magnetic field lines in Earth's magnetosheath from in-situ spacecraft measurements. *Journal of Geophysical Research: Space Physics*, *127*(12), e2022JA030996. https://doi.org/10.1029/2022JA030996

NěmečekZ., ĎurovcováT., ŠáfrankováNěmecF., MatteiniL., StansbyD., JanitzekN., et al. (2020). What is the solar wind frame of reference? *The Astrophysical Journal*, *889*(2), 163. https://doi.org/10.3847/1538-4357/ab65f7

Phan, T.-D., Paschmann, G., Baumjohann, W., Sckopke, N., & Lühr, H. (1994). The magnetosheath region adjacent to the dayside magnetopause: AMPTE/IRM observations. *Journal of Geophysical Research*, *99*(1), 121–141. https://doi.org/10.1029/gm090p0115

Pudovkin, M. I., Besser, B. P., Zaitseva, S. A., Lebedeva, V. V., & Meister, C.-V. (2001). Magnetic barrier in case of a southward interplanetary magnetic field. *Journal of Atmospheric and Solar-Terrestrial Physics*, *63*(10), 1075–1083. https://doi.org/10.1016/s1364-6826(01)00023-2

Pudovkin, M. I., & Semenov, V. S. (1985). Magnetic field reconnection theory and the solar wind—Magnetosphere interaction: A review. *Space Science Reviews*, *41*(1–2), 1–89. https://doi.org/10.1007/bf00241346

Romashets, E. P., & Vandas, M. (2019). Analytic modeling of magnetic field in the magnetosheath and outer magnetosphere. *Journal of Geophysical Research: Space Physics*, *124*(4), 2697–2710. https://doi.org/10.1029/2018JA026006

Shue, J.-H., Chao, J. K., Fu, H. C., Russell, C. T., Song, P., Khurana, K. K., & Singer, H. J. (1997). A new functional form to study the solar wind control of the magnetopause size and shape. *Journal of Geophysical Research*, *102*(5), 9497–9951. https://doi.org/10.1029/97JA00196

Spreiter, J. R., & Rizzi, A. W. (1974). Aligned magnetohydrodynamic solution for solar wind flow past the Earth's magnetosphere. *Acta Astronautica*, *1*(1–2), 15–35. https://doi.org/10.1016/0094-5765(74)90006-x

Trattner, K. J., Petrinec, S. M., & Fuselier, S. A. (2021). The location of magnetic reconnection at Earth's magnetopause. *Space Science Reviews*, *217*(3), 41. https://doi.org/10.1007/s11214-021-00817-8

Tsyganenko, N., Andreeva, V., Kubyshkina, M., Sitnov, M., & Stephens, G. (2021). Data-based modeling of the Earth's magnetic field. In R. Maggiolo, N. André, H. Hasegawa, & D. Welling (Eds.), *Magnetospheres in the solar system, geophysical monograph 259*. Wiley & Sons, Inc. https://doi.org/10.1002/9781119815624.ch.39

Tsyganenko, N., Semenov, V., & Erkaev, N. (2023). Data-based modeling of the magnetosheath magnetic field [Dataset]. Zenodo. (Funded by the Russian Science Foundation grant 23-47-00084). https://doi.org/10.5281/zenodo.8416108

Tsyganenko, N. A., & Andreeva, V. A. (2016). An empirical RBF model of the magnetosphere parameterized by interplanetary and ground-based drivers. *Journal of Geophysical Research: Space Physics*, *121*(11), 10786–10802. https://doi.org/10.1002/2016JA023217

Zhang, H., Fu, S., Pu, Z., Lu, J., Zhong, J., Zhu, C., et al. (2019). Statistics on the magnetosheath properties related to magnetopause magnetic reconnection. *The Astrophysical Journal*, *880*(2), 122. https://doi.org/10.3847/1538–4357/ab290e